
Mind the Gap:

Navigating Inference with Optimal Transport Maps

Malte Algren (malte.algren@unige.ch), **Tobias Golling** (tobias.golling@unige.ch)
University of Geneva

Francesco Armando Di Bello (francescoarmando.dibello@unige.it)
INFN and University of Genova

Christopher Pollard (christopher.pollard@warwick.ac.uk)
University of Warwick

Abstract

Machine learning (ML) techniques have recently enabled enormous gains in sensitivity across the sciences. In particle physics, much of this progress has relied on excellent simulations of a wide range of physical processes. However, due to the sophistication of modern machine learning (ML) algorithms and their reliance on high-quality training samples, discrepancies between simulation and experimental data can significantly limit the effectiveness of ML techniques. In this work, we present a solution to this “mis-specification” problem: a calibration approach based on optimal transport, which we apply to high-dimensional simulations for the first time. We demonstrate the performance of our approach through jet tagging, using a CMS-inspired dataset. A 128-dimensional internal jet representation from a powerful general-purpose classifier is studied; after calibrating this internal “latent” representation, we find that a wide variety of quantities derived from it for downstream tasks are also properly calibrated: using this calibrated high-dimensional representation, powerful new applications of jet flavor information can be utilized in LHC analyses. This is a key step toward allowing properly-calibrated “foundation models” in particle physics. More broadly, this calibration framework has broad applications for correcting high-dimensional simulations across the sciences.

1 Introduction

Model mis-specification occurs when the process of generating observations does not belong to the family of statistical models used for inference. This is a growing issue across disciplines: the physical sciences, economics, social sciences, medicine and health. As the use of inference techniques built on complex and precise statistical models, often enabled by sophisticated simulations, becomes more widespread, it is critical to develop techniques that mitigate mis-specification, enabling inference that is both effective and unbiased.

In hierarchical models, the likelihood of observing some datum x , given a parameter of interest θ , is determined by marginalizing over any stochastic latent variable ω : $p(x|\theta) = \int d\omega p(x|\omega, \theta) p(\omega|\theta)$. An important subset of hierarchical models comprises those which factorize, such that x only depends on θ through ω , i.e. $p(x|\omega, \theta) = p(x|\omega)$. In such situations, it may be possible to calculate $p(x|\omega)$ separately, or to constrain it via auxiliary experiments. Indeed, this is often the motivation for constructing the likelihood $p(x|\theta)$ in terms of a latent ω : when $p(x|\theta) \approx \int d\omega p(x|\omega) p(\omega|\theta)$, then both $p(x|\omega)$ and $p(\omega|\theta)$ can be independently derived or verified.

Inference on approximately factorizable likelihoods is especially powerful. Scientific instruments are often designed to measure a quantity x independent of the details of the particular experiment, aside from a latent variable ω . For example, when measuring the weight of an object, an ideal scale is one that provides an accurate and precise estimate of the object’s weight, $p(x = \text{estimated weight}|\omega = \text{true weight})$, independently of whether the object is, say, a penguin or a banana ($\theta = \{\text{penguin, banana}\}$). A scale with this factorization property can be calibrated independently using a set of test objects whose weights are well-known. In doing so, the experimenter constructs a good approximation of the scale’s density over outputs for a known input; this can be used to infer the weight of a variety of objects: penguins, bananas, or otherwise.

In practice, likelihoods often do not factorize exclusively through some stochastic latent ω that can be measured in calibration experiments, but they depend on a variety of additional stochastic latents ω' . In such cases, it is not possible to derive the full dependence $p(x|\omega, \omega')$, but it may still be possible to *correct* the explicit dependence on ω .

We are aware of two procedures for deriving these corrections to the simulated density, $p_{\text{sim}}(x|\omega)$, with calibration measurements, $p_{\text{data}}(x|\omega)$. The first constructs the density ratio

$$s_{\omega}(x) \equiv \frac{p_{\text{data}}^{\text{CR}}(x|\omega)}{p_{\text{sim}}^{\text{CR}}(x|\omega)} \quad (1)$$

using observations in a “calibration region” (CR). Inference on θ is then performed on observations in the “signal region” (SR) using the corrected likelihood

$$p(x|\theta) = \int d\omega d\omega' s_{\omega}(x) p_{\text{sim}}(x|\omega, \omega') p_{\text{sim}}(\omega, \omega'|\theta). \quad (2)$$

Thus, corrections derived in the CR are applied in the SR via the weight $s_{\omega}(x)$; this is colloquially known as “vertical calibration”.

An alternative strategy is to derive the conditional transport function T_ω (and corresponding transport map $(T_\omega)_\#$) such that

$$(T_\omega)_\# p_{\text{sim}}^{\text{CR}}(x|\omega) \equiv p_{\text{sim}}^{\text{CR}}(T_\omega x|\omega) = p_{\text{data}}^{\text{CR}}(x|\omega). \quad (3)$$

This transport is subsequently applied in the SR, resulting in the corrected likelihood

$$p(x|\theta) = \int d\omega d\omega' (T_\omega)_\# p_{\text{sim}}(x|\omega, \omega') p_{\text{sim}}(\omega, \omega'|\theta). \quad (4)$$

This “horizontal calibration” moves the simulated observations based on what is observed in the calibration region. The suitable transport map for correcting simulations is the *optimal* one, i.e. the one which minimally alters $p_{\text{sim}}(x|\omega)$ for each choice of ω while still closing with $p_{\text{data}}(x|\omega)$. The optimal transport (OT) map is solution to this closure problem that is least invasive, in the sense that it preserves the full structure of $p_{\text{sim}}(x|\omega, \omega')$ as well as possible.

It is worth noting that, in the limit that ω captures all the mismodeling of the simulation $p_{\text{sim}}(x|\omega, \omega')$, then the corrected simulation converges to the “true” likelihood p_{data} . This is true for both vertical and horizontal strategies. While it is not the focus of this article, the choice of ω against which one parameterizes the corrections is important; enabling corrections that are so *conditioned* on a maximally-informative ω , of potentially very high-dimensions, is an active field of research.

In the past several years, ML-based solutions to both the vertical and horizontal calibration problems have been developed. Density ratio estimation (DRE) via neural-network (NN) classifiers is a well-established technique that scales well to high dimensions in both x and ω [1]. More recently, neural OT solvers have been introduced [2–5], enabling the derivation of optimal transport maps for horizontal calibrations of multi-dimensional simulations from which samples can be drawn [6, 7].

As we scale into higher dimensions, it is important to recognize that the horizontal and vertical strategies are distinct solutions to the calibration problem and exhibit different behaviors. In sample-based simulations, the reweighting function $s_\omega(x)$ used in vertical calibration will, in general, dilute the statistical power of the simulated samples by a factor

$$\rho_\omega = \frac{1}{N} \frac{(\sum_i^N s_\omega(x_i))^2}{\sum_i^N s_\omega(x_i)^2}. \quad (5)$$

Horizontal calibration does not introduce a dilution. Indeed, for well-behaved spaces (e.g. Euclidean space), a horizontal solution to a given calibration problem always exists; for vertical calibrations, a solution only exists if $\forall x \omega. p_{\text{data}}(x|\omega) > 0 \Rightarrow p_{\text{sim}}(x|\omega) > 0$, i.e. the simulated distribution fully supports the data distribution and s_ω is always finite. These properties originate from the fact that an optimal transport *distance* between densities p and q over a space Y is well-defined under rather loose conditions on Y [8], while vertical calibrations inherently depend on the KL-*divergence* between p and q to be finite [9].

In this article we explore a concrete example of an important calibration problem in particle physics. Data analysis in High Energy Physics (HEP) experiments at the Large Hadron Collider (LHC) aims to study the fundamental properties of matter by analyzing the complex final states resulting from high-energy collisions. These analyses rely on a hierarchical stochastic calculations, where simulations of the underlying “hard process,” involving fundamental particles, approximately factorize

from the subsequent evolution into stable particles that eventually interact with the detector, whose signals undergo sequential processing through a series of algorithms defining the reconstruction chain of the experiment.

Ultimately, a dedicated analysis is conducted to extract key parameters of the underlying theoretical models of interest, θ , which govern the initial hard process. Within this framework, Monte Carlo (MC) simulations play a crucial role in modeling the likelihood via sampling. Although MC simulations are grounded in first-principles, they often exhibit substantial discrepancies when compared to experimental data, rendering $p_{\text{sim}}(x|\omega)$ unreliable at the required precision.

Given that these probability distributions are inherently intractable, controlling every potential source of mismodeling from first principles is impractical. Instead, dedicated calibration regions are defined and corrections derived. The conditioning variables ω often comprise kinematic properties related to the reconstructed observable x .

Here we focus on an important use-case that is ubiquitous across the LHC physics programme: characterizing jets of hadronic particles (“jets”). For example, establishing what was the origin of a jet observed in a detector is critical for a broad number of important conclusions drawn from LHC data. ML techniques have vastly improved our ability to answer this question to high precision in recent years [10, 11].

Recently, foundation models have emerged as promising tools for enhancing reconstruction tasks, summarizing the relevant features of jets in a general way [12–14].

Foundation models used for jet tagging are essentially large-scale transformer-based networks that can be pre-trained to encode high-dimensional representations of jets, z . These latent representations may then be used as inputs for downstream inference tasks. While foundation models offer significant potential for enhancing HEP reconstruction pipelines, experimental methodologies for calibrating discrepancies between MC simulations and real experimental data in the latent representation are currently lacking. In this work, we build upon previous research and, for the first time, introduce a calibration approach leveraging optimal transport theory, applied directly in a high-dimensional latent space of up to 128 dimensions. Calibration algorithms based on optimal transport have been introduced in Ref. [6, 7] and applied to correct low-dimensional data representations, such as the output scores of classifiers used for jet tagging in Ref. [11, 15]. While we demonstrate this methodology in the context of jet tagging, its applicability extends to a wide range of reconstruction tasks in HEP experiments.

This article describes two primary contributions in this direction. First, we find that density ratio-based calibrations are not suitable in our real-world case, because the densities between our base model and simulated data are not sufficiently overlapping. Second, we find that optimal-transport solutions to the calibration problem scale up to high dimensionality and properly close in an inference-relevant way.

2 Related work

Optimal transport (OT) has recently emerged as a powerful tool for constructing high dimensional maps between distributions, with a growing body of applications in both theoretical and experimental physics [16–19].

In high-energy physics (HEP), one of the primary applications of OT is to correct discrepancies in simulated datasets through calibration [6]. This approach has been adopted by the ATLAS experiment, which employed OT to calibrate algorithms used for b -jet identification [7]. To the best of the author’s knowledge, this represents the first instance of a horizontal calibration method applied to jet tagging. In contrast, conventional jet-tagging calibration techniques predominantly rely on vertical calibration strategies [15, 20–23].

OT has also been explored in the modeling of complex background processes in the context of double Higgs bosons production at the LHC [24], for anomaly detection algorithms [25], and for variable decorrelation [26].

These advances are grounded in foundational developments by Monge and Kantorovich [8], as well as in algorithmic contributions that enabled scalable applications of OT in machine learning [27].

3 Simulated dataset

The dataset utilized in this study is based on `JetClass` [28], a well-established benchmark for jet classification tasks in HEP. It is generated using standard Monte Carlo event generators widely adopted in LHC experiments and incorporates detector response and reconstruction effects simulated with DELPHES [29] (v3.4.2).

Jet reconstruction is performed using the anti- k_T clustering algorithm [30, 31] with a radius parameter of $R = 0.8$, applied to the E-Flow objects reconstructed by DELPHES. The analysis focuses on jets with transverse momenta in the range of 500–1000 GeV and pseudorapidity satisfying $|\eta| < 2$.

Each jet in the dataset is assigned to one of ten distinct classes (l), corresponding to the underlying physics processes responsible for its production. These classes include Higgs boson decays ($H \rightarrow b\bar{b}$, $H \rightarrow c\bar{c}$, $H \rightarrow gg$, $H \rightarrow 4q$), top quark decays ($t \rightarrow bq\bar{q}'$, $t \rightarrow b\ell\nu$), hadronic decays of W and Z bosons, and a background class labeled q/g , which represents jets originating from light quarks (u, d, s) or gluons (g): $l \in Hbb, Hcc, Hgg, H4q, Hl\nu qq, tbq\bar{q}', t\bar{b}l\nu, Wqq, Zqq, q/g$.

This study focuses on the calibration of q/g jets which are abundantly produced at the LHC. The samples are generated using QCD multijet processes simulated with `Pythia` v8.186 [32]. Parton showering and hadronization are also modeled with the same generator. Additionally, multiple parton interactions are included in the simulation, while pile-up effects are not considered.

To emulate the typical discrepancies observed between simulated samples and real collision data in LHC experiments, two datasets of QCD multijet events are generated. The first dataset, referred to as the *source*, is produced using the standard `JetClass` configuration. The second dataset, referred

to as the *target*, is created by modifying the smearing functions of the DELPHES detector simulation. In particular, the impact parameters of charged particles are additionally smeared by 10%–30%, based on informed estimates from Ref. [33]. In parallel, the renormalization and factorization scales of the QCD multijet events are increased from 1 to 2. These modifications are intended to simulate two main sources of systematic differences: inaccuracies in the modeling of the underlying physical processes, and effects stemming from detector response and reconstruction. Figure 1 compares the distributions of the transverse impact parameter (d_0) and the number of jet constituents for the two datasets.

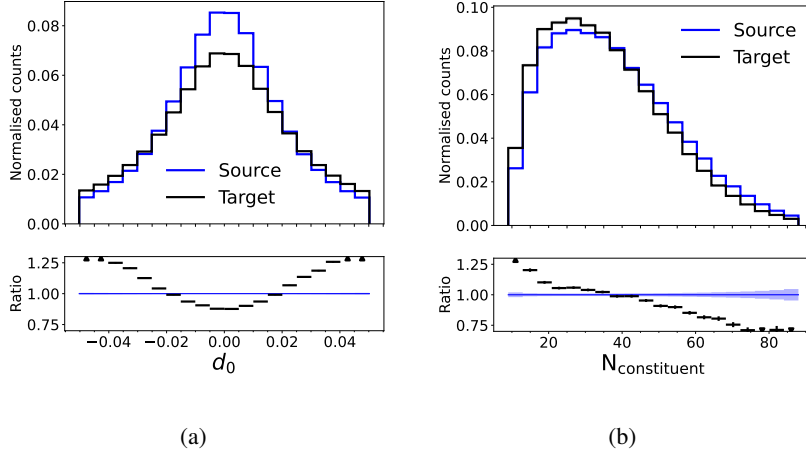


Figure 1: The distributions are represented as follows: source distribution (blue) and target distribution (black). (a) shows the change in the transverse impact parameter (d_0), while (b) illustrates the change in number of constituents ($N_{\text{constituent}}$) between the datasets.

4 Method

4.1 Constructing the classifier

The identification of jet origin, commonly referred to as jet tagging, is a key challenge in particle physics, where machine learning techniques have become increasingly prominent. In this work, we construct a classifier based on a transformer [34] architecture that closely resembles the state-of-the-art models currently employed for jet-tagging at LHC experiments [10, 11].

The classifier is designed to estimate the conditional probability distribution for the origin of a jet, $p(l \mid \{\vec{c}_{\text{obs}}\}, \text{jet}_{\text{obs}})$, where \vec{c}_{obs} denotes the set of features associated with the jet constituents, and jet_{obs} is a fixed-size vector of jet-level observables, including the pseudorapidity η , azimuthal angle ϕ , transverse momentum p_T , energy E , and constituent multiplicity N . A complete list of input variables, along with their corresponding distributions, is provided in Appendix C.

The classifier uses a dedicated *ClassToken* [35] to aggregate the input set \vec{c}_{obs} into a fixed 512-dimensional latent representation. The Transformer encoder is composed of multiple stacked lay-

ers, each consisting of a multi-head self-attention mechanism followed by a feed-forward neural network [34]. The jet input features jet_{obs} are integrated into the encoder via Feature-wise Linear Modulation (FiLM), following the methodology established in Ref. [36].

The jet's latent representation is passed to the output multi-layer perceptron head (MLP Head), which consists of a sequence of linear layers with GELU activation functions [37], each maintaining a fixed latent dimensionality of 128. The final output of the network is a 10-dimensional latent vector containing the unnormalized class scores (logits) corresponding to the different jet categories. An overview of the classifier architecture is shown in Fig. 2. The first 128-dimensional layer of the MLP Head, denoted z_{128} , is the target of the calibration. The final 128-dimensional layer (z'_{128}) and the output layer (z'_{10}) are also shown in Fig. 2 with dashed lines, and are used in the evaluation of the calibration procedure, as further discussed in Section 5.

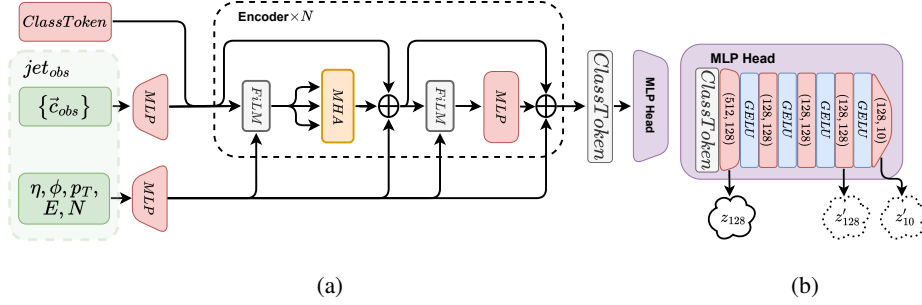


Figure 2: The two diagrams show (a) the transformer encoder and (b) the output multi-layer perceptron head (MLP Head). The transformer architecture incorporates a sequence of encoder layers [38], each comprising multi-head self-attention mechanisms (MHA) [34] followed by feed-forward neural networks (MLP) [39] with Feature-wise Linear Modulation (FiLM) [36, 40] for conditional integration. The MLP Head consists of a sequence of linear transformations and GELU [37] with a final output size of 10 for the class probabilities.

The model is trained using the publicly available JetClass dataset [28]. Details of the training procedure are provided in Appendix B.

4.2 Deriving the optimal transport map

The primary objective of this work is to derive an optimal transport map, denoted by \hat{T}_ω , such that

$$(\hat{T}_\omega)_\# p_{\text{sim}}(z_{128} \mid \omega) = p_{\text{data}}(z_{128} \mid \omega), \quad (6)$$

where p_{sim} and p_{data} represent the distributions of the latent representation z_{128} in simulation and real data, respectively, conditioned on ω . The conditioning variable ω typically includes jet kinematic features such as $\text{jet-}p_T$, $\text{jet-}\eta$, and other relevant labels extracted from the simulated dataset. In this work we neglect dependencies on the jet kinematics and thus restrict ω to the q/g label of the simulated sample that we aim to calibrate.

The optimal transport map \hat{T}_ω is a unique transformation that minimally distorts p_{sim} in order to match p_{data} . Refs. [2–5, 7, 26] have shown that \hat{T}_ω can be learned by minimizing the Euclidean transport cost between the simulated and observed data distributions, using a pair of input-convex neural networks (ICNNs) [41]. This approach is formalized by the following optimization problem:

$$W_2^2(z, y) = \sup_{f(y) \in \text{cvx}(y)} \inf_{g(z) \in \text{cvx}(z)} f(\nabla_z g(z)) - \langle z, \nabla_z g(z) \rangle - f(y), \quad (7)$$

Where f and g are two distinct input-convex neural networks (ICNNs), and $z \sim p_{\text{sim}}$ and $y \sim p_{\text{data}}$ denote samples from the simulated and target distributions, respectively. For simplicity, we have omitted the subscript 128 from z and y .

At convergence, the optimal transport map is given by $\hat{T}_\omega(z|\omega) = \nabla_z g(z|\omega)$, which maps simulated latent representations z to their calibrated counterparts y , conditioned on ω . Further details on the ICNN architecture and training procedure are provided in Appendices A and B.

5 Results

5.1 Evaluating closure in the latent space

To visualize the impact of calibration within the high-dimensional latent space z_{128} , Principal Component Analysis (PCA) [42] is applied to reduce the dimensionality to the five leading principal components. The distributions of these components are presented as corner plots in Fig. 3.

Fig. 3(a) illustrates the presence of the expected discrepancies between the source (simulated) and target (synthetic) data distributions. After applying the optimal transport map, Fig. 3(b) shows a significant reduction in these discrepancies, indicating successful alignment between the latent representations of the two domains.

The calibration procedure is further evaluated using discriminators, denoted \mathcal{D}_L , trained to distinguish between the source and target distributions across the initial 128-dimensional layer (z_{128}), the final 128-dimensional layer (z'_{128}), and the output layer (z'_{10}) of the MLP Head. Fig. 4(a) presents the receiver operating characteristic (ROC) curves of \mathcal{D}_L trained on each of these layers. As expected, discrepancies between the source and target distributions are largest in z_{128} and decrease progressively in deeper layers, with the smallest differences observed in z'_{10} .

After applying the calibration to the source distribution, the discriminator ability to separate source from target is substantially diminished. A minor residual discrepancy persists in z_{128} but vanishes in the deeper layers, resulting in area under the curve (AUC) values of 0.5 in the z'_{128} and z'_{10} latent spaces.

The discriminant score produced by \mathcal{D}_L in the z_{128} latent space is presented in Fig. 4(b). The source and target distributions exhibit only limited overlapping support and are otherwise nearly disjoint. In such cases, calibration methods based on reweighting—referred to as vertical calibration in the

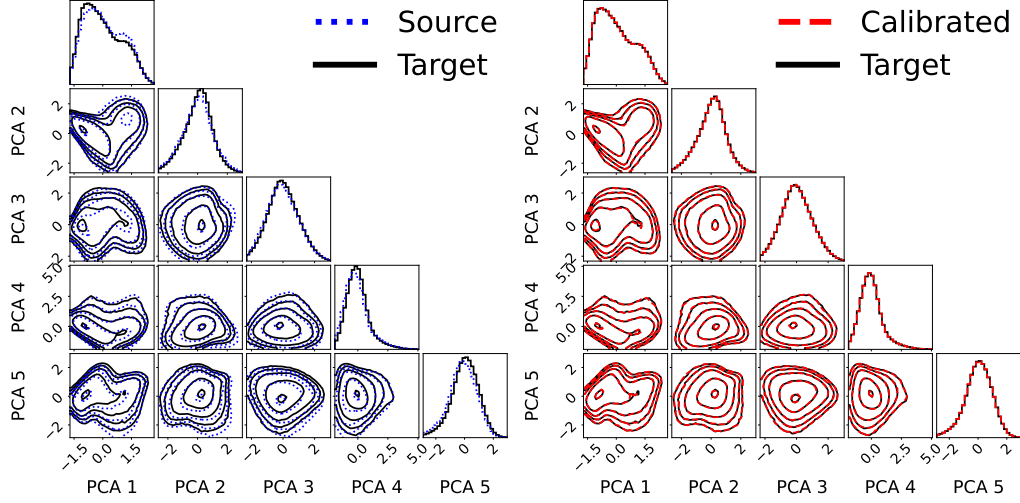


Figure 3: Corner plots of the first five principal components derived from PCA applied to the z_{128} latent space. The 2D contours show 5%, 50%, 80%, 90%, and 95% percentiles. (a) Comparison between the target distribution (black) and the source distribution (blue). (b) Comparison between the target distribution (black) and the calibrated distribution (red). The calibration is derived in z_{128} , and subsequent layers in the MLP Head are applied to map it to the 10-dimensional output space.

introduction are subject to substantial statistical inefficiency due to the sparse overlap, thereby limiting their applicability. By contrast, the proposed horizontal calibration approach is not hindered by the lack of distributional overlap and thus remains a feasible strategy to calibrate high dimensional latent representations.

To further evaluate the performance of the calibration procedure, discriminators are trained to distinguish between the calibrated and target distributions within the latent spaces z_{128} , z'_{128} and z'_{10} . Notably, the discriminator achieves an AUC close to unity in the z_{128} latent space, indicating that either residual discrepancies persist post-calibration or new mismatches are introduced during the calibration process. However, in the z'_{128} layer, the AUC decreases to approximately 0.5, suggesting that these discrepancies are effectively attenuated by the subsequent transformations within the classifier. This result implies that residual discrepancies in the z_{128} latent space do not propagate to the downstream layers and are therefore inconsequential for the final classification task.

To validate this, the impact of the calibration is further examined in the classifier's output space. In typical applications output probabilities are combined to construct log-likelihood discriminants. Fig. 5 displays the distributions of these discriminants, where Higgs boson decays to b - or c -quark pairs are considered signal, while multijet and top-quark events define the background hypothesis.

Prior to calibration, clear discrepancies is observed between the source (blue) and target (black) distributions. As expected, the application of the calibration procedure (red) substantially reduces these differences, indicating improved agreement between the two distributions.

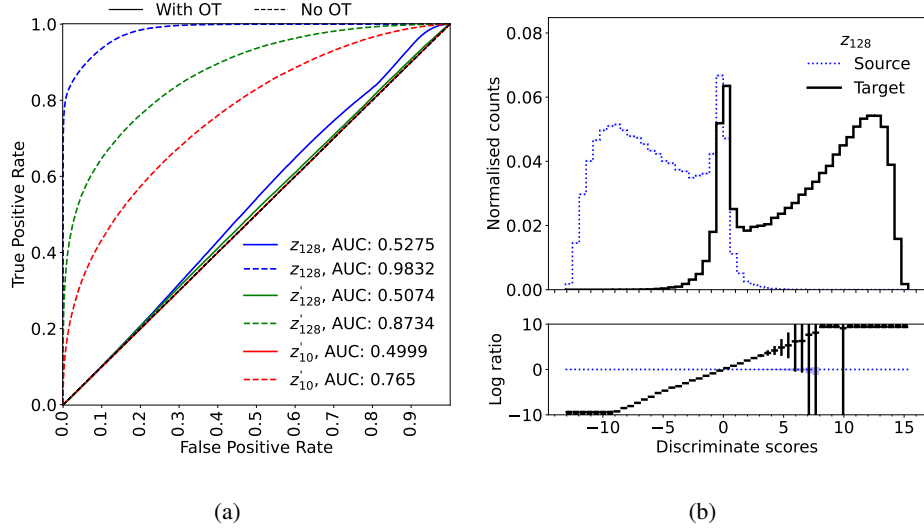


Figure 4: (a) Receiver operating characteristic (ROC) curves for discriminators \mathcal{D}_L trained to differentiate between source and target distributions across three representational spaces: the 128-dimensional latent space (z_{128}), the final 128-dimensional layer in the MLP Head (z'_{128}), and the 10-dimensional output space (z'_{10}). The discriminators are subsequently evaluated on the calibrated versus target distributions, where an area under curve (AUC) value approximating 0.5 indicates successful mitigation of distributional discrepancies that were previously exploited by the discriminator. (b) Marginal distribution of the discriminators \mathcal{D}_L scores in z_{128} , between the source (blue) and target (black) distributions.

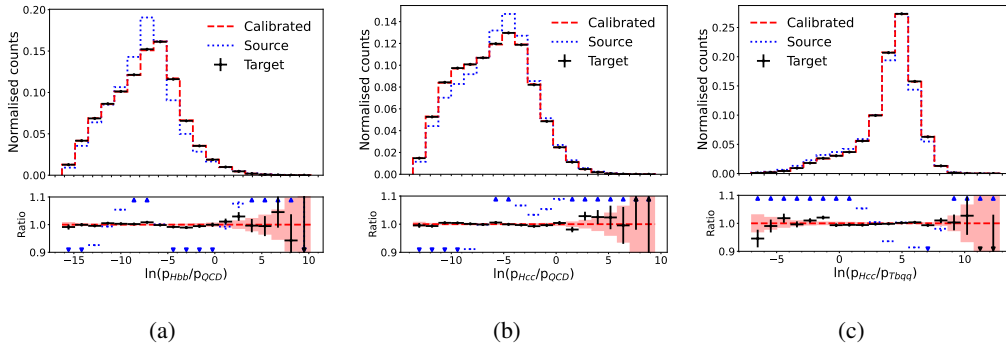


Figure 5: Comparisons between the marginal distributions of the physics-motivated one-dimensional discriminants. The distributions are represented as follows: target distribution (black), calibrated distribution (red), and source distribution (blue). The calibration is derived on the z_{128} latent space, and then the subsequent MLP Head layers are applied to map it to the output space. Afterwards the output space is projected onto physics-motivated one-dimensional discriminants.

6 Conclusion

A calibration strategy based on optimal transport has been presented, targeting latent representations within transformer-based classifiers used in high-energy particle physics. By applying the calibration directly in the high-dimensional latent space, rather than on low-dimensional observables or classifier outputs, the proposed method enables more flexible and detailed correction of mismodeling effects present in simulated data. This approach also establishes a foundation for the direct calibration of large, pre-trained models in physics applications.

Quantitative evaluations using discriminator networks indicate that the calibrated latent representations can achieve good agreement with the target domain for physics-relevant inference tasks. While this work focuses on jet classification, the methodology is broadly applicable to a range of reconstruction tasks in high-energy physics that utilize deep learning models.

Acknowledgements

The MA and TG would like to acknowledge funding through the SNSF Sinergia grant CR-SII5_193716 “Robust Deep Density Models for High-Energy Particle Physics and Solar Flare Analysis (RODEM)” and the SNSF project grant 200020_212127 “At the two upgrade frontiers: machine learning and the ITk Pixel detector”. CP acknowledges support through STFC consolidated grant ST/W000571/1.

Appendix

A Optimal transport

Optimal transport theory addresses the fundamental problem of determining an efficient mapping between probability distributions, specifically between source distribution Q and target distribution P . Following the notation established in the introduction, we denote $Q = p_{\text{sim}}$ and $P = p_{\text{data}}$. The concept of optimality is in relation to minimizing of a cost function $c(x, y)$, which quantifies the price of transporting density between p_{sim} and p_{data} .

The classical primal formulation of the optimal transport problem [43], is defined as:

$$T^* = \inf_{T: T_{\#} p_{\text{sim}} = p_{\text{data}}} \frac{1}{2} \mathbb{E}_{X \sim p_{\text{sim}}} [\|z - T(z)\|^2], \quad (8)$$

where T is the transport map and $\|\cdot\|$ is the cost function that ranks the maps. It is an optimization problem that seeks to find the map T that minimizes $\|\cdot\|$ over all maps that satisfy $T_{\#} p_{\text{sim}} = p_{\text{data}}$, where $T_{\#}$ is the pushforward operator [8]. Monge’s transport maps are defined as deterministic maps, which imposes significant analytical challenges [8, 44]. Consequently, Kantorovich proposed a relaxation of Monge’s primal formulation by conceptualizing transport as a probability measure rather than a deterministic mapping [44]. Additionally to the relaxation, Kantorovich introduced a dual problem that has the same solution as the primal one. The dual problem is defined as:

$$W_2^2(f, g) = \sup_{f(y) + g(z) \leq c(y, z)} \mathbb{E}_{Y \sim p_{\text{sim}}} [f(y)] + \mathbb{E}_{Z \sim p_{\text{data}}} [g(z)], \quad (9)$$

where f and g are functions subject to the constraint $f(y) + g(z) \leq c(y, z)$ [8]. Ref. [2] demonstrated that for continuous distributions, the optimal transport can be derived through the following optimization problem:

$$W_2^2(y, z) = \sup_{f(y) \in \text{cvx}(y)} \inf_{g(z) \in \text{cvx}(z)} f(\nabla_z g(z)) - \langle z, \nabla_z g(z) \rangle - f(y), \quad (10)$$

where $f(y)$ and $g(z)$ are convex functions over the respective domains. The resulting optimal transport map is characterized as $T^* = \nabla_z g(z)$, which maps points from the source domain to the target domain.

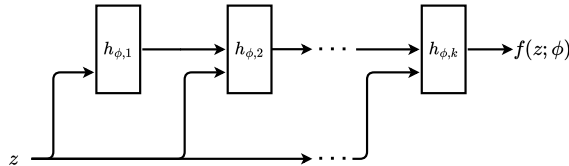


Figure 6: The diagram shows the architecture of the ICNN[41] used to derive the optimal transport by optimizing Eq. (10). The specific implementation of the ICNN that is used in this paper follows the architecture described in [3, 26].

A.1 Method to derive the optimal transport

As established in Appendix A, the solution to Eq. (10) requires two convex functions f and g . While conventional neural networks (NN) are not limited to convex functions, Ref. [41] introduced input-convex neural networks (ICNNs), which limit the parametrization of NNs to only convex functions $f(y; \theta)$ with respect to their input variables y . The ICNN architecture implements a recursive formulation across layers $i = 0, \dots, k - 1$, wherein the i^{th} layer is defined as:

$$h_{i+1} = \sigma(W_i^h h_i + W_i^y y + b_i), \quad f(y; \theta) = h_k, \quad (11)$$

where $h_0 = W_i^h = 0$, and σ represents a convex, monotonically non-decreasing activation function. A schematic representation of the ICNN architecture is illustrated in Fig. 6.

There is an extensive literature on the ICNN and using it to derive the optimal transport [2–5, 7, 26] with different tweaks to the ICNN architecture and the training procedure.

The specific architecture and training implementation of the ICNNs used in this paper follow the architecture of Ref. [3] and training procedure of Ref. [26].

B Hyperparameters

B.1 Classifier trained on the JetClass dataset

Transformer based classifier trained on JetClass dataset. The output of the classifier is a 10-dimensional vector representing the probability of the jet belonging to one of the 10 classes. The classifier was trained with 100,000 optimizer steps of AdamW [45] with a learning rate of 10^{-4} and a warmup of 10,000 steps. The full hyperparameters of the classifier are listed in Table 1.

B.2 Hyperparameters of the ICNN

Two ICNN networks are used to derive the optimal transport map, both with the same hyperparameters, which are listed in Table 2. The ICNNs are trained on source and target samples of size 8,181,000, with a validation size of 909,000 for each source and target. The latent space is standardized to have zero mean and unit variance before being passed to the ICNNs.

B.3 Hyperparameters of the classifiers used for evaluation \mathcal{D}_L

In the evaluation stage of the latent space calibration, a classifier is trained to The classifier \mathcal{D}_L is the classifier used to distinguish between the target and source distributions and calibrated and target. The hyperparameters of \mathcal{D}_L are listed in Table 3. The total number of parameters in \mathcal{D}_L is around a 1 million.

Train	Number of epochs	4
	Gradient clipping	1.0
	LR scheduler	Warmup(10^{-4} , 10000)
	Batch size	1000
	Optimizer	AdamW
Transformer	d_{model}	512
	Dropout	0.1
	Number of encoders	4
	MLP	GLU
	Dimension increase in MLP	$\times 2$
	Attention head	8
MLP Head	Number of layers	5
	Activation function	GELU

Table 1: Hyperparameters of the classifier trained on JetClass. Diagram of the architecture can be seen in Fig. 2.

nICNN	Number of blocks	4
ICNN block	Number of layers	2
	Hidden dimension	2048
	Activation function	Zeroed Softplus
	Optimizer	AdamW
Train	LR Scheduler	CosineAnnealingLR($5 \cdot 10^{-4}$, 10^{-7})
	Optimizer	AdamW
	f per g	4
	g per f	10
	Steps per epoch	512
	Epochs	1000
	Batch size	1024

Table 2: Hyperparameters of the ICNNs used to derive the optimal transport map.

\mathcal{D}_L network	Number of layers	4
	Hidden dimension	512
	Activation function	SiLU
	Normalization	LayerNorm
	Optimizer	AdamW
Train	LR Scheduler	CosineAnnealingLR(10^{-4} , 10^{-7})
	Early stopping	100
	Epochs	200
	Batch size	1024

Table 3: Hyperparameters of the classifier \mathcal{D}_L used to discriminate between source vs target and calibrated vs target distributions.

C Input variables

Tables 4 and 5 list the features of the particles and jets in the JetClass dataset used to train the classifier.

Continuous features	
Transverse momentum	p_T
Pseudorapidity to the jet axis	$\Delta\eta$
Azimuthal angle to the jet axis	$\Delta\phi$
Transverse impact parameter	d_0
Longitudinal impact parameter	z_0
Uncertainty on d_0	σ_{d_0}
Uncertainty on z_0	σ_{z_0}
Particle type index	
Photon	0
Negative hadron	1
Neutral Hadron	2
Positive Hadron	3
Electron	4
Positron	5
Muon	6
Anti-muon	7

Table 4: Features of the particle constituents of the jets in the JetClass dataset. The preprocessing of the features followed the procedure described in Ref [12].

Scalar features	
Jet transverse momentum	p_T
Jet pseudorapidity	η
Jet azimuthal	ϕ
Jet multiplicity	N
Jet energy	E

Table 5: Features associated with a jet in the JetClass dataset. The preprocessing of the features followed the procedure described in Ref [12].

Figs. 7 and 8 show the marginal distributions of the input features normalized with *QuantileTransformer*.

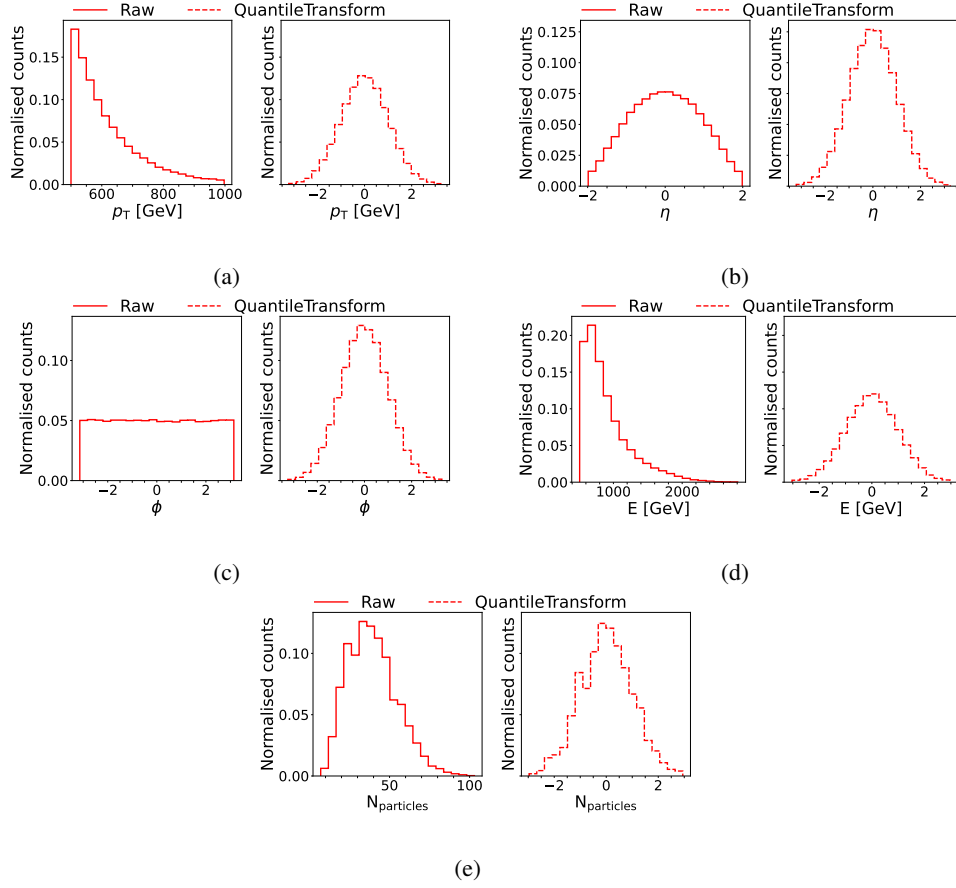


Figure 7: Marginal distributions of the JetClass jet features used as input to the classifier. Each figure shows the marginal distribution of a single jet feature and the quantile-transformed feature. The quantile-transformed feature is used as input to the classifier.

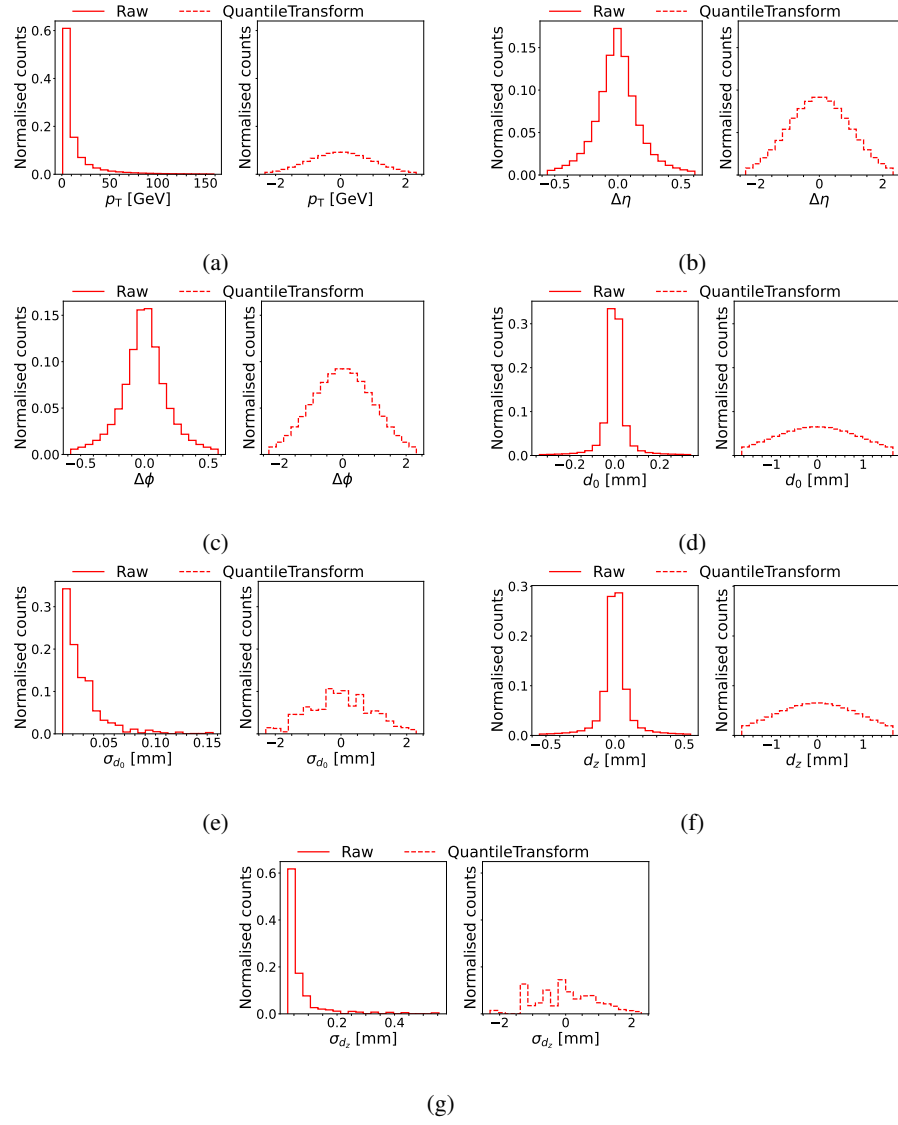


Figure 8: Marginal distributions of the JetClass constituent features used as input to the classifier. Each figure shows the marginal distribution of a single constituent feature and the quantile-transformed feature. The quantile-transformed feature is used as input to the classifier. For some features, they are not defined for neutral particles. In those features the neutrals are removed.

D Results

D.1 Calibrated results for MLP Head

Fig. 9 show the ROC curves of the discriminators trained to discriminate between the calibration and target distributions, as well as the nominal and target distributions. Fig. 10 show the marginal

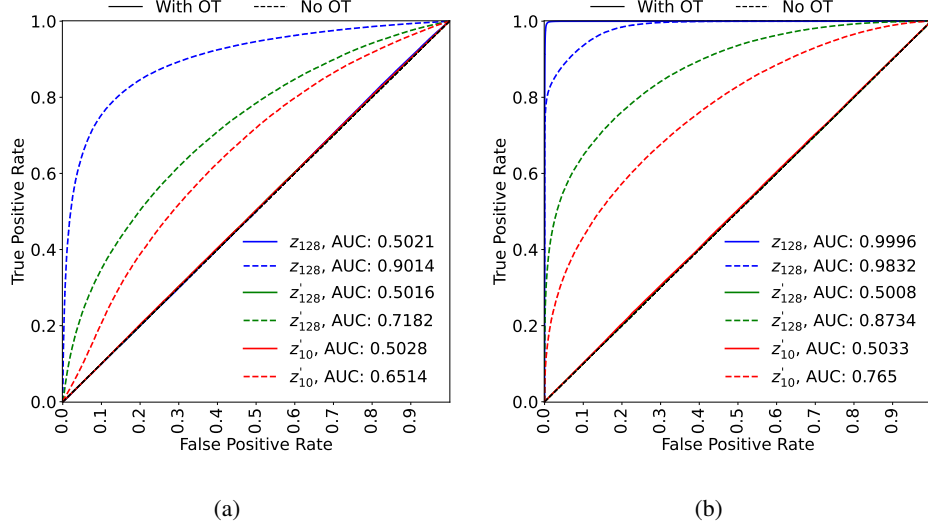


Figure 9: ROC curves of discriminators trained on the z_{128} , z'_{128} and z'_{10} latent space. Here the calibration has been derived in z_{128} and the later layers in the MLP Head have been applied to map it to z'_{128} and z'_{10} . Given the linestyle of the ROC curves, the discriminators are either trained to distinguish between the calibration and the target or nominal vs target. Each AUC is also included in the legend. (a) shows the ROC curves of a single linear layer classifier. (b) shows the ROC curves of \mathcal{D}_L .

distributions of the output space of the classifier, comparing the target distribution, the transported distribution, and the source distribution. Fig. 11 shows an additional physics motivated discriminator.

D.2 Corner plots in the output space

Figs. 12 and 13 show the corner plots of the output space of the classifier with and without calibration.

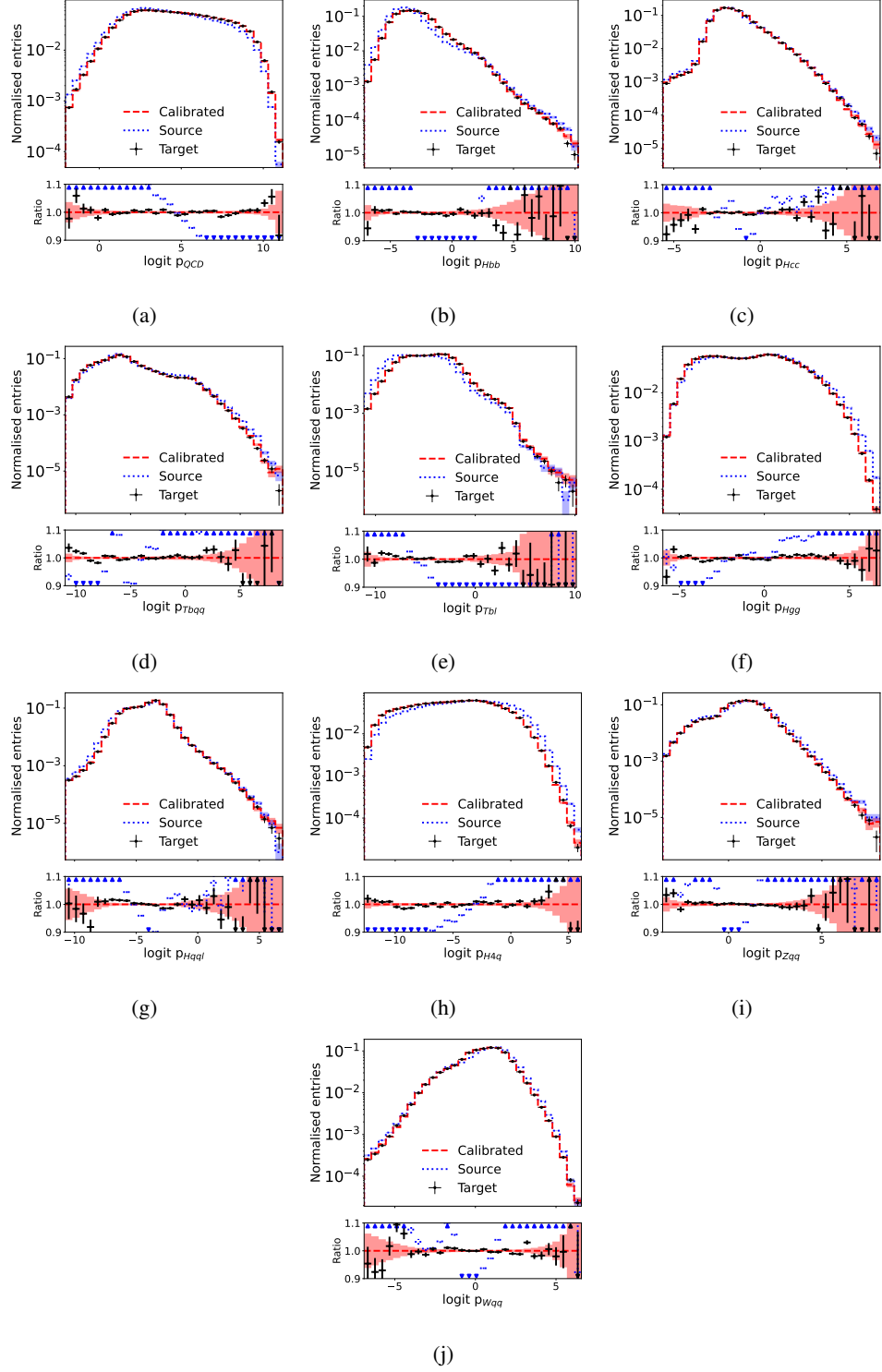
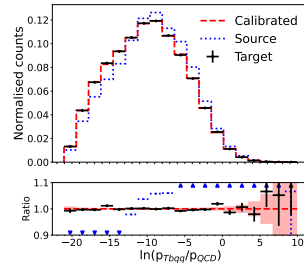


Figure 10: Comparisons of the marginal distributions of the output space z'_{10} of the classifier. The black distribution represents target distribution, red is the transported distribution and blue is the source distribution. The transport has been derived in z_{128} and the later layers in the MLP Head have been applied to map it to z'_{10} . Closure of the calibration is indicated by the difference to the black distribution.



(a)

Figure 11: Comparison between the marginal distributions of a physics-motivated one-dimensional discriminants. The distributions are represented as follows: target distribution (black), calibrated distribution (red), and source distribution (blue). The calibration is derived on the z_{128} latent space, then the subsequent MLP Head layers are applied to map it to output space z'_{10} where Softmax is applied to map the output space to a simplex. Afterwards the output space is projected to physics-motivated one-dimensional discriminants.

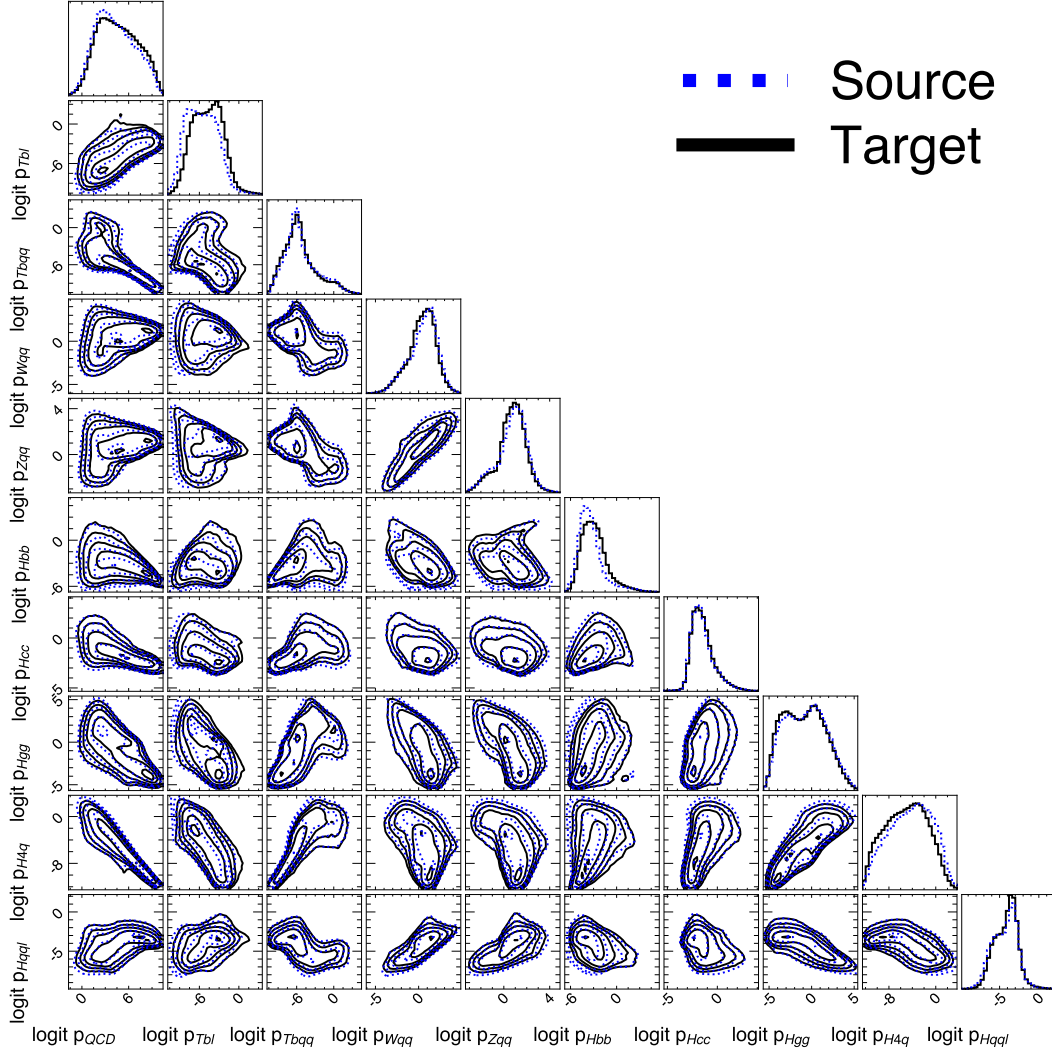


Figure 12: Comparisons of the marginal distribution of the output space z'_{10} of the classifier. The black distribution represents target distribution, red is the transported distribution and blue is the source distribution. The transport has been derived in z_{128} and the later layers in the MLP Head have been applied to map it to z'_{10} . Closure of the calibration is indicated by the difference to the black distribution.

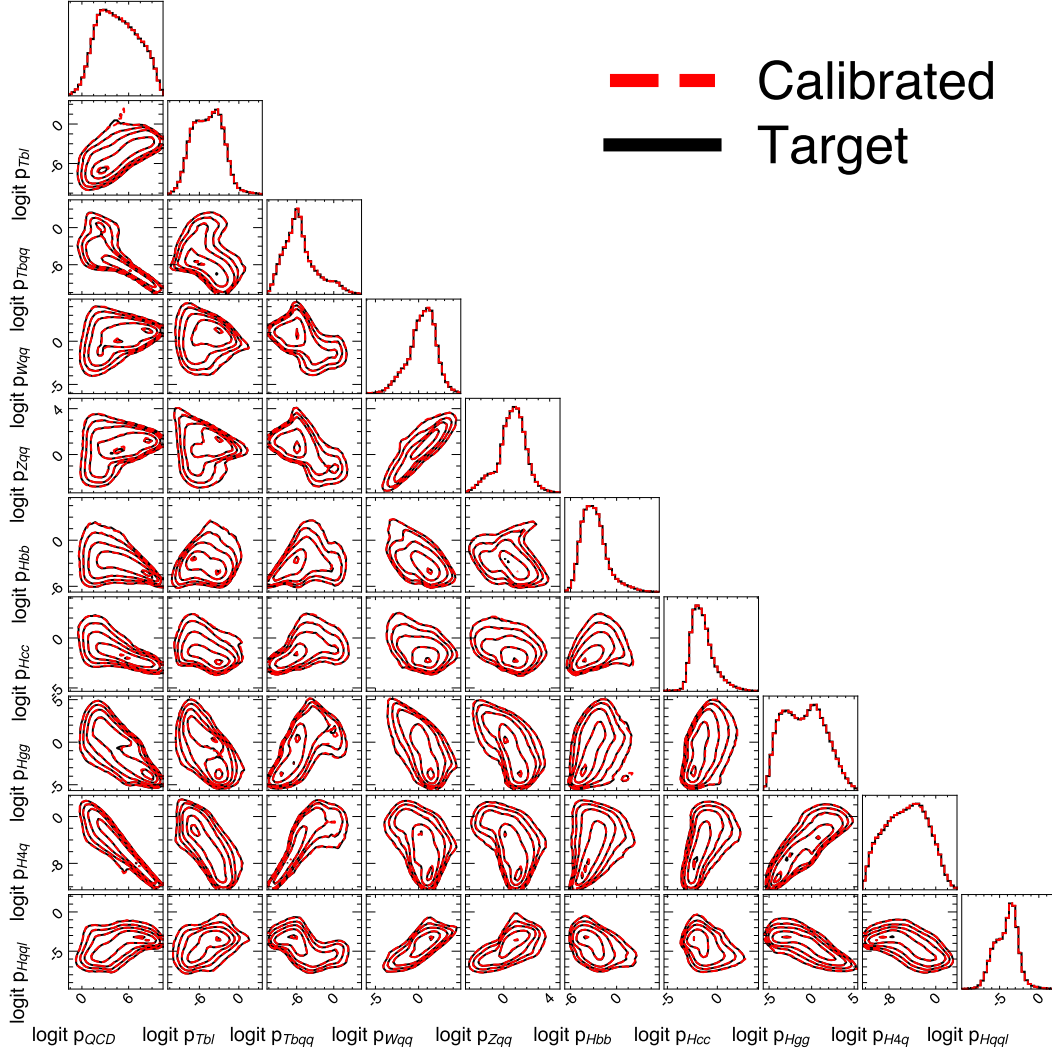


Figure 13: Comparisons of the marginal distribution of the output space z'_{10} of the classifier. The black distribution represents target distribution, red is the transported distribution and blue is the source distribution. The transport has been derived in z_{128} and the later layers in the MLP Head have been applied to map it to z'_{10} . Closure of the calibration is indicated by the difference to the black distribution.

References

- [1] Cranmer, K., Pavez, J., and Louppe, G. *Approximating Likelihood Ratios with Calibrated Discriminative Classifiers*. In: *Machine Learning: Science and Technology* 5.3 (2024), p. 035073. arXiv: 1506.02169 [stat.AP]. URL: <https://arxiv.org/abs/1506.02169>.
- [2] Makkuva, A. V. et al. *Optimal transport mapping via input convex neural networks*. In: *CoRR* abs/1908.10962 (2019). arXiv: 1908.10962. URL: <http://arxiv.org/abs/1908.10962>.
- [3] Huang, C.-W. et al. *Convex Potential Flows: Universal Probability Distributions with Optimal Transport and Convex Optimization*. 2021. arXiv: 2012.05942 [cs.LG]. URL: <https://arxiv.org/abs/2012.05942>.
- [4] Korotin, A. et al. *Do Neural Optimal Transport Solvers Work? A Continuous Wasserstein-2 Benchmark*. In: *CoRR* abs/2106.01954 (2021). arXiv: 2106.01954. URL: <https://arxiv.org/abs/2106.01954>.
- [5] Bunne, C., Krause, A., and Cuturi, M. *Supervised Training of Conditional Monge Maps*. 2023. arXiv: 2206.14262 [cs.LG]. URL: <https://arxiv.org/abs/2206.14262>.
- [6] Pollard, C. and Windischhofer, P. *Transport away your problems: Calibrating stochastic simulations with optimal transport*. In: *Nuclear Instruments and Methods in Physics Research Section A: Accelerators, Spectrometers, Detectors and Associated Equipment* 1027 (Mar. 2022), p. 166119. ISSN: 0168-9002. URL: <http://dx.doi.org/10.1016/j.nima.2021.166119>.
- [7] ATLAS Collaboration. *A continuous calibration of the ATLAS flavour-tagging classifiers via optimal transportation maps*. In: (2025). arXiv: 2505.13063 [hep-ex]. URL: <https://arxiv.org/abs/2505.13063>.
- [8] Villani, C. *Optimal Transport: Old and New*. Grundlehren der mathematischen Wissenschaften. Springer Berlin Heidelberg, 2008. ISBN: 9783540710509. URL: https://books.google.ch/books?id=hV8o5R7_5tkC.
- [9] Goodfellow, I., Bengio, Y., and Courville, A. *Deep Learning*. <http://www.deeplearningbook.org>. MIT Press, 2016.
- [10] CMS Collaboration. *A unified approach for jet tagging in Run 3 at $\sqrt{s} = 13.6$ TeV in CMS*. In: *CMS-DP-2024-066* (2024). URL: <https://cds.cern.ch/record/2904702>.
- [11] ATLAS Collaboration. *Transforming jet flavour tagging at ATLAS*. In: *arXiv preprint* (May 2025). arXiv: 2505.19689 [hep-ex].
- [12] Leigh, M. et al. *Is Tokenization Needed for Masked Particle Modelling?* 2024. arXiv: 2409.12589 [hep-ph]. URL: <https://arxiv.org/abs/2409.12589>.
- [13] Li, C. et al. *Accelerating Resonance Searches via Signature-Oriented Pre-training*. 2024. arXiv: 2405.12972 [hep-ph]. URL: <https://arxiv.org/abs/2405.12972>.

- [14] Birk, J., Hallin, A., and Kasieczka, G. *OmniJet- α : the first cross-task foundation model for particle physics*. In: *Machine Learning: Science and Technology* 5.3 (Aug. 2024), p. 035031. ISSN: 2632-2153. URL: <http://dx.doi.org/10.1088/2632-2153/ad66ad>.
- [15] ATLAS Collaboration. *ATLAS b -jet identification performance and efficiency measurement with $t\bar{t}$ events in pp collisions at $\sqrt{s} = 13$ TeV*. In: *Eur. Phys. J. C* 79.11 (2019), p. 970. URL: <https://doi.org/10.1140/epjc/s10052-019-7450-8>.
- [16] Brenier, Y., Frisch, U., et al. *Reconstruction of the initial conditions of the Universe by optimal mass transportation*. In: *MNRAS* 329 (2002), p. 903. eprint: astro-ph/0109483.
- [17] Lévy, A., Brenier, Y., and Mohayaee, R. *Monge–Ampère gravity: A new framework for cosmological structure formation*. In: *UnivEarthS Lab Highlights* (2022). URL: <https://www.iap.fr/actualites/laune/2022/TransportOptimal/OptimalTransport-en.html>.
- [18] Hausegger, S. von, Lévy, A., and Mohayaee, R. *Accurate reconstruction of the baryon acoustic oscillation scale with optimal transport*. In: *Phys. Rev. Lett.* 129.25 (2022), p. 251101.
- [19] Jasche, J. et al. *Optimal Transport as a Subhalo Abundance Matching Method*. In: *arXiv preprint* (2024). arXiv: 2502.17553 [astro-ph.CO].
- [20] CMS Collaboration. *Identification of heavy, energetic, hadronically decaying particles using machine-learning techniques*. In: *JINST* 15.06 (2020), P06005. URL: <https://doi.org/10.1088/1748-0221/15/06/P06005>.
- [21] ATLAS Collaboration. *Efficiency corrections for a tagger for boosted $H \rightarrow b\bar{b}$ decays in pp collisions at $\sqrt{s} = 13$ TeV with the ATLAS detector*. ATLAS Note. CERN, Aug. 2021. URL: <https://cds.cern.ch/record/2777811>.
- [22] ATLAS Collaboration. *Performance of Top Quark and W Boson Tagging in Run 2 with ATLAS*. ATLAS Note. All figures including auxiliary figures are available at the CDS record. Geneva: CERN, Aug. 2017. URL: <https://cds.cern.ch/record/2281054>.
- [23] CMS Collaboration. *A new calibration method for charm jet identification validated with proton–proton collision events at $\sqrt{s} = 13$ TeV*. In: *JINST* 17.03 (2022), P03014. URL: <https://doi.org/10.1088/1748-0221/17/03/P03014>.
- [24] Manole, T. and al., et. *Background Modeling for Double Higgs Boson Production: Density Ratios and Optimal Transport*. In: (2022). arXiv: 2208.02807 [stat.AP].
- [25] Craig, N., Howard, J., and Li, H. *Exploring Optimal Transport for Event-Level Anomaly Detection at the Large Hadron Collider*. In: (2024). arXiv: 2401.15542 [hep-ph].
- [26] Algren, M., Raine, J. A., and Golling, T. *Decorrelation using optimal transport*. In: *The European Physical Journal C* 84.6 (June 2024). ISSN: 1434-6052. URL: <http://dx.doi.org/10.1140/epjc/s10052-024-12868-6>.
- [27] Peyré, G. and Cuturi, M. *Computational Optimal Transport*. In: *Foundations and Trends in Machine Learning* 11.5–6 (2019), pp. 355–607. arXiv: 1803.00567.

- [28] Qu, H., Li, C., and Qian, S. *JetClass: A Large-Scale Dataset for Deep Learning in Jet Physics*. Version 1.0.0. Zenodo, June 2022. URL: <https://doi.org/10.5281/zenodo.6619768>.
- [29] Favereau, J. de et al. *DELPHES 3: a modular framework for fast simulation of a generic collider experiment*. In: *Journal of High Energy Physics* 2014.2 (Feb. 2014). ISSN: 1029-8479. URL: [http://dx.doi.org/10.1007/JHEP02\(2014\)057](http://dx.doi.org/10.1007/JHEP02(2014)057).
- [30] Cacciari, M., Salam, G. P., and Soyez, G. *The anti-ktjet clustering algorithm*. In: *Journal of High Energy Physics* 2008.04 (Apr. 2008), pp. 063–063. ISSN: 1029-8479. URL: <http://dx.doi.org/10.1088/1126-6708/2008/04/063>.
- [31] Cacciari, M., Salam, G. P., and Soyez, G. *FastJet user manual: (for version 3.0.2)*. In: *The European Physical Journal C* 72.3 (Mar. 2012). ISSN: 1434-6052. URL: <http://dx.doi.org/10.1140/epjc/s10052-012-1896-2>.
- [32] Sjöstrand, T. et al. *An introduction to PYTHIA 8.2*. In: *Computer Physics Communications* 191 (June 2015), pp. 159–177. ISSN: 0010-4655. URL: <http://dx.doi.org/10.1016/j.cpc.2015.01.024>.
- [33] ATLAS Collaboration. *Calibration of light-flavour b-jet mistagging rates using ATLAS proton–proton collision data at $\sqrt{s} = 13$ TeV*. Tech. rep. Geneva: CERN, 2018. URL: <https://cds.cern.ch/record/2314418>.
- [34] Vaswani, A. et al. *Attention Is All You Need*. In: *CoRR* abs/1706.03762 (2017). arXiv: 1706.03762. URL: <http://arxiv.org/abs/1706.03762>.
- [35] Devlin, J. et al. *BERT: Pre-training of Deep Bidirectional Transformers for Language Understanding*. In: *CoRR* abs/1810.04805 (2018). arXiv: 1810.04805. URL: <http://arxiv.org/abs/1810.04805>.
- [36] Peebles, W. and Xie, S. *Scalable Diffusion Models with Transformers*. 2023. arXiv: 2212.09748 [cs.CV]. URL: <https://arxiv.org/abs/2212.09748>.
- [37] Hendrycks, D. and Gimpel, K. *Bridging Nonlinearities and Stochastic Regularizers with Gaussian Error Linear Units*. In: *CoRR* abs/1606.08415 (2016). arXiv: 1606.08415. URL: <http://arxiv.org/abs/1606.08415>.
- [38] Xiong, R. et al. *On Layer Normalization in the Transformer Architecture*. In: *CoRR* abs/2002.04745 (2020). arXiv: 2002.04745. URL: <https://arxiv.org/abs/2002.04745>.
- [39] Shazeer, N. *GLU Variants Improve Transformer*. 2020. arXiv: 2002.05202 [cs.LG]. URL: <https://arxiv.org/abs/2002.05202>.
- [40] Perez, E. et al. *FiLM: Visual Reasoning with a General Conditioning Layer*. Dec. 2017. eprint: 1709.07871 (cs). (Visited on 01/21/2025).
- [41] Amos, B., Xu, L., and Kolter, J. Z. *Input Convex Neural Networks*. In: *CoRR* abs/1609.07152 (2016). arXiv: 1609.07152. URL: <http://arxiv.org/abs/1609.07152>.

- [42] Shlens, J. *A Tutorial on Principal Component Analysis*. In: *CoRR* abs/1404.1100 (2014). arXiv: 1404.1100. URL: <http://arxiv.org/abs/1404.1100>.
- [43] Monge, G. *Mémoire sur la théorie des déblais et des remblais*. Imprimerie royale, 1781. URL: <https://books.google.ch/books?id=IG7CGwAACAAJ>.
- [44] Kantorovich, L. *On the Translocation of Masses*. In: *Journal of Mathematical Sciences* 133 (2006), pp. 1381–1382. URL: <https://api.semanticscholar.org/CorpusID:122853046>.
- [45] Loshchilov, I. and Hutter, F. *Fixing Weight Decay Regularization in Adam*. In: *CoRR* abs/1711.05101 (2017). arXiv: 1711.05101. URL: <http://arxiv.org/abs/1711.05101>.